Giuseppe Di Florio | Erik Bründermann | Nataraja Sekhar Yadavalli
Svetlana Santer | Martina Havenith

Polarized 3D Raman and nanoscale near-field optical microscopy of optically inscribed surface relief gratings

chromophore orientation in azo-doped polymer films

Suggested citation referring to the original publication:
Soft Matter 10 (2013), pp. 1544–1554
DOI http://dx.doi.org/10.1039/c3sm51787j

Soft Matter

PAPER

View Article Online
View Journal | View Issue

Cite this: *Soft Matter*, 2014, **10**, 1544

Polarized 3D Raman and nanoscale near-field optical microscopy of optically inscribed surface relief gratings: chromophore orientation in azo-doped polymer films†

Giuseppe Di Florio,*[a] Erik Bründermann,[a] Nataraja Sekhar Yadavalli,[b] Svetlana Santer[b] and Martina Havenith[a]

Received 30th June 2013
Accepted 5th December 2013

DOI: 10.1039/c3sm51787j

www.rsc.org/softmatter

We have used polarized confocal Raman microspectroscopy and scanning near-field optical microscopy with a resolution of 60 nm to characterize photoinscribed grating structures of azobenzene doped polymer films on a glass support. Polarized Raman microscopy allowed determining the reorientation of the chromophores as a function of the grating phase and penetration depth of the inscribing laser in three dimensions. We found periodic patterns, which are not restricted to the surface alone, but appear also well below the surface in the bulk of the material. Near-field optical microscopy with nanoscale resolution revealed lateral two-dimensional optical contrast, which is not observable by atomic force and Raman microscopy.

1 Introduction

Properties of polymers adsorbed onto a solid surface deviate from bulk behavior, due to the presence of two interfaces that play an important role in the observed material properties, *e.g.* the glass transition temperature (T_g).[1–3] The understanding of the physicochemical properties must include the interphase behaviour, *i.e.* the variation of the polymer component distribution vertically and laterally, if the films are multi-component systems. Thin polymer systems influenced by one or more interfaces can express new and unexpected material properties. Molecular organization of the polymer components highly influences the final properties. Control of the microstructure enables us to tailor and design new materials.

Azobenzene chromophores used as polymer chain side groups have found widespread applications, because changes in morphology can be triggered optically. Polymer systems containing azo-dyes have been investigated as potential smart materials for various optical applications, *e.g.* data storage media,[4–6] alignment layers for liquid crystalline fluorescent polymers in display and semiconductor technology,[7,8] waveguides and waveguide couplers,[9] transducing optical information[10] and nonlinear optics.[11]

Patterned modifications can be achieved during irradiation of azobenzene containing thin polymer films with interference patterns (IPs) produced by two interfering laser beams. During such irradiation the polymer film deforms following intensity or polarization distribution in the incoming beam forming the so called surface relief gratings (SRGs). The shape of the SRGs is typically sinusoidal with the width in the range of several hundreds of nanometers (restricted by diffraction limits) and a few micrometers, and the height can be up to several micrometers.

These gratings generally show a high diffraction efficiency.[12–17] The formation of the grating is connected with mass migration of the polymer chains governed by a large extent of photo-induced reorientation of the azobenzene molecules.[17–24,33] The multiple photoisomerization (Fig. 1) of azobenzene groups during irradiation allows for reorientation preferentially perpendicular with their main axis to the electrical field vector.[18–21,23]

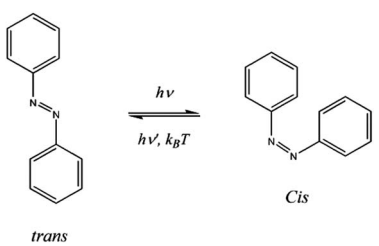

Fig. 1 Photoisomerization of azobenzene by linear polarized light.

[a]Ruhr-Universität Bochum, Physical Chemistry II, Universitätsstr. 150, 44780 Bochum, Germany. E-mail: martina.havenith@rub.de

[b]Universität Potsdam, Institute for Physics and Astronomy, Karl-Liebknecht-Str. 24/25, 14476 Potsdam-Golm, Germany

† Electronic supplementary information (ESI) available. See DOI: 10.1039/c3sm51787j

Although several physical models have been developed to elucidate the molecular origin of the forces and mechanism involved in chain migration upon light irradiation, this molecular mechanism is still a matter of controversy.[25–32]

Some models propose that a pressure gradient emerging during light exposure is responsible for grating formation on the material surface. The laser interference pattern in the material determines regions with different photochemical responses: regions with high photoisomerization are accompanied by regions of low photoisomerization, thus leading to a pressure gradient. The chain migration is considered as a result of a viscoelastic flow from high to low pressure regions.[29]

A different mechanism has been proposed by Pedersen *et al.* who introduced a mean-field potential[27] taking into account the intermolecular interactions of aligned azobenzene-dyes responsible for mass transport.[27]

In the present study we have characterized photosensitive polymer films containing azo-moieties spin coated onto glass slides. The films have been illuminated here from the back side in order to generate a surface grating on the front side of the films.

We have investigated the response of the photosensitive material under different conditions. We apply polarized confocal Raman spectroscopy to study local orientation of azobenzene groups within photosensitive polymer films as a function of position on and inside SRGs.

Polarized confocal Raman spectroscopy is a very sensitive technique to achieve information about molecular orientations and distributions. Here, Raman spectroscopy is coupled with a confocal microscope to achieve spatial three-dimensional resolution, which allows studying the organization of molecular domains at a micrometer level. We have investigated the samples to determine the molecular orientations within the surface pattern following an approach by Sourisseau and co-workers.[33–37]

In the present study, to the best of our knowledge, we have used for the first time optical sectioning in the third dimension measuring the polymer film with surface relief gratings in order to characterize the material properties and the molecular orientational effects. Additionally, we have employed scanning near-field optical microscopy (SNOM) to probe the material optical properties with nanometer resolution, which revealed unexpected lateral two-dimensionally modulated optical contrast.

We show that a deeper understanding at a molecular level of the mechanisms acting during light exposure can be obtained by 3D high resolution microscopy characterizing mass migration on the free surface of the optically inscribed grating, and in addition in the bulk of the material.

2 Experimental set-up

The measurements have been conducted on samples of PAZO (poly[1-[4(3-carboxy-4-hydroxyphenylazo)benzenesulfonamido]-1,2-ethanediyl, sodium salt]) photosensitive polymer films. Thin films of 1 μm thickness have been produced by spin coating on glass slides. The molecular structure of the azobenzene containing polymer is shown in Fig. 2.

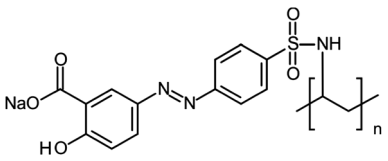

Fig. 2 Structure of the used azo-polymer PAZO (poly[1-[4(3-carboxy-4-hydroxyphenylazo)benzenesulfonamido]-1,2-ethanediyl, sodium salt]).

The surface relief gratings have been inscribed by irradiating the samples with two interfering beams, using a laser at a wavelength of 488 nm with an intensity of 70 mW (Fig. 3). The laser beam is split into two beams and then recombined on the samples with a certain angle of incidence. In this study we investigated two gratings inscribed by polarization interference patterns (PIPs) with ±45° polarization of two interfering beams (Fig. 4(a)) and with SP polarization (Fig. 4(b)). The local orientation of the electric field vector during the surface relief grating formation with different interference patterns is studied in detail elsewhere.[38,39] The surface relief grating period was kept

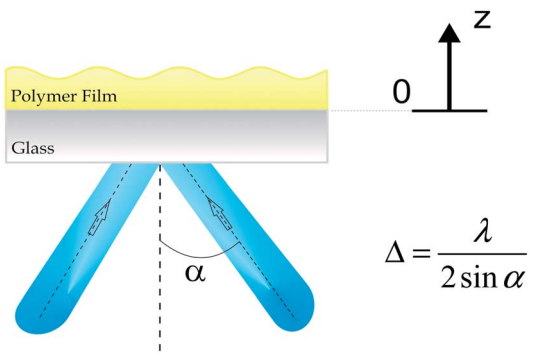

Fig. 3 Sketch of the azo-polymer samples. The back side illumination produces a grating on the opposite side of the film with a period Δ. Here λ denotes the laser wavelength.

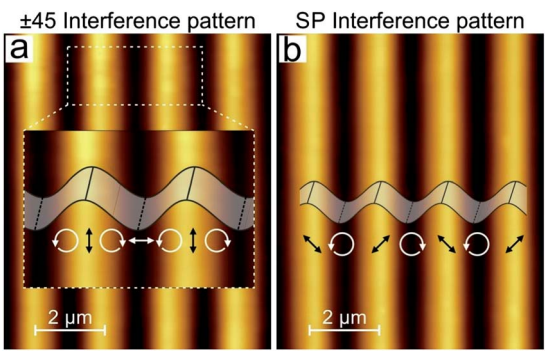

Fig. 4 AFM micrographs of the SRGs inscribed by polarization interference patterns of two combinations: (a) ±45° polarization of two interfering beams, and (b) SP polarization combinations. The distribution of the electrical field vector relative to the position of maxima and minima of the grating is added as well.

constant for all measurements (2 μm). Fig. 4 shows the distribution of the electrical field vector within the interference pattern as a function of the position on the grating topography. In the case of ±45° polarization, we found the maxima of the topography at vertical polarization, while the minima were found at horizontal polarization. The SP interference pattern results in the formation of a grating where each linearly polarized pattern induces maxima in topography.

Raman spectra and images with a lateral resolution of about 500 nm have been recorded using a confocal Raman microscope using a 100×/0.9 NA objective (model alpha300 RAS, WITec GmbH, Ulm, Germany). The photoexcitation laser used for the measurements has a wavelength of 785 nm, which is well outside the absorption band of the chromophores.

The spectral range from 140 to 3750 cm^{-1} was covered with a resolution of <4 cm^{-1} (Fig. 5).

The power was restricted to 20 mW in order to avoid any thermal or bleaching effects. We have confirmed that no degradation or bleaching of the samples was found during the measurements. A polarizer was placed in the path of the incident Raman laser that allows control of the direction of the laser polarization vector. The laser light is focused on the sample and the scattered radiation is collected by the same objective in a backscattering configuration. Rayleigh scattered photons are minimized by a filter. The Raman photons pass through an analyzer in order to select the polarization of the photons that reach the detection system. The samples were mounted on a motorized stage (which has a precision of 1 nm in *x*–*y*) with the grooves of the diffraction grating being parallel to the *Y* axis of the stage. Fig. 4 shows the spatial variation of the polarization state of the field, which originates from the superposition of the two pump beams.[40]

Polarized Raman spectra and images have been recorded in two experimental set-ups. At first, the Raman laser polarization vector is configured along the *Y* axis, which is parallel to the grooves of the grating. In this configuration the Raman intensities I_{yy} and I_{yx} are measured. I_{ij} denotes the intensity which is scattered in the *j* direction (analyzer aligned along *j*) after excitation by the laser with a polarization vector pointing along the *i* direction (polarizer aligned along *i*).

In the second configuration the Raman laser polarization vector is directed along the *X* axis, *i.e.* perpendicular to the grooves of the grating. Here the Raman intensities I_{xx} and I_{xy} can be measured.

The Raman images have been collected using a stepwise increase of 0.25 μm in both *X* and *Y* directions and an integration time of 0.5 s per spectrum. Images of a total sample size 15 μm × 10 μm have been recorded. A second set of Raman images of size 12 μm × 1 μm has been recorded using a scan step size of 0.2 μm in *X* and *Y* and 1 s per spectrum.

Optical sections of the sample have been collected with a 0.2 μm scan step in both *X* and *Z* directions and a size of 10 μm in *X* and 5 μm in *Z* directions. The Raman map consists of a number of line scans, covering several grating periods, each acquired at a fixed *Z*-position. The focus of the confocal Raman microscope was scanned along the *Z*-direction (Fig. 3) until a depth the Raman signals could not be recorded anymore.

For SNOM measurements the instrument is equipped with a hollow pyramid tip on a cantilever that acts, simultaneously, as an AFM sensor and an optical probe (model alpha300 RAS, WITec GmbH, Ulm, Germany). The pyramid presents a hole at the apex with an aperture of about 60 nm that defines the lateral resolution of the near-field measurement. The SNOM images have been acquired in contact-mode. The signal is collected in transmission mode: the excitation laser (785 nm the same as for Raman measurements) is focused onto the pyramid tip and the transmitted light is collected by an inverted objective and directed to an avalanche photodiode detector (APD).

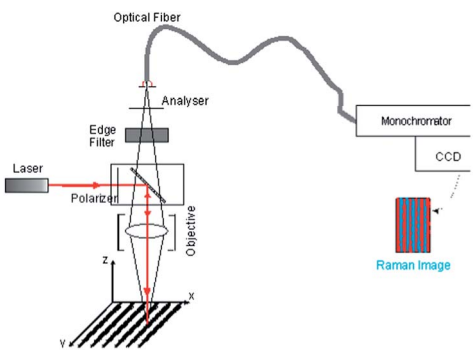

Fig. 5 Experimental set-up and laboratory coordinate system.

3 Theoretical background

Experimental techniques such as polarized Raman, infrared dichroism, anisotropy of broad-line NMR can be used to characterize the anisotropy induced by various forming processes (drawing, extrusion, *etc.*). In many cases the results of measurements give access to averaged orientational quantities.[41,42] However, here we want to address the question which microscopic distribution corresponds to the measured averages.[43–45] We briefly outline the formalism to analyze the polarized Raman data. More details used in the analysis can be found in the ESI.†

We limit the discussion to systems where the population of chromophores with cylindrical symmetry shows a uniaxial distribution of orientations with respect to the direction of the external force perturbing the isotropy of the system.[46]

For any isotropic or anisotropic medium averaged orientational quantities can be obtained[46–48]:

$$I_{\mathrm{Raman}(I,J)} \approx \left\langle (\alpha_{IJ})^2 \right\rangle = \frac{1}{8\pi^2} \int_0^{2\pi} \mathrm{d}\psi \int_0^{2\pi} \mathrm{d}\varphi \int_{-1}^{+1} F(\psi, \varphi, \cos\theta)[T^t \alpha T]^2 \mathrm{d}(\cos\theta) \quad (1)$$

$F(\psi, \varphi, \cos\theta)$ describes the so-called orientation distribution function (ODF). In a uniaxial system, which contains molecules of cylindrical symmetry, $F(\theta)$ will be independent of φ and ψ. $F(\theta)\mathrm{d}\Omega$ represents the fraction of molecules whose axis is within the solid angle $\mathrm{d}\Omega$ at an angle θ to the aligning direction.

In our experiments, the population of chromophores follows an alignment process perpendicularly to the polarization vector of the interference beam by means of isomerization and reorientation cycles. The final ODF only depends on the polar angle θ and can be approximated as the sum of even order Legendre polynomials:[44,46,49]

$$F(\theta) = \sum_{l=0,2,4} \left(\frac{2l+1}{2}\right) \langle P_l \rangle P_l(\cos\theta) \quad (2)$$

with the order parameters $\langle P_l \rangle$ being defined as:

$$\langle P_0 \rangle = 1 \quad (3a)$$

$$\langle P_2 \rangle = \frac{1}{2}\left(3\langle \cos^2\theta \rangle - 1\right) \quad (3b)$$

$$\langle P_4 \rangle = \frac{1}{8}\left(35\langle \cos^4\theta \rangle - 30\langle \cos^2\theta \rangle + 3\right) \quad (3c)$$

The knowledge of the averages $\langle \cos^2\theta \rangle$ and $\langle \cos^4\theta \rangle$, or equivalently of the order parameters gives direct information on the chromophore ODF.

The inscribed SRG can be described by a sinusoidal function with a phase $\delta = \frac{2\pi X}{\Lambda}$, with Λ being the period of the grating. An additional rotation $R(\beta)$ about the Z axis takes into account different positions with respect to the grating.

This allows the calculation of the experimental intensity ratios $R_1(\delta) = \frac{I_{yx}}{I_{yy}}$ and $R_2(\delta) = \frac{I_{xy}}{I_{xx}}$. Subsequently, the averaged quantities $\langle \cos^2\theta \rangle$, $\langle \cos^4\theta \rangle$, $\langle P_2 \rangle$, and $\langle P_4 \rangle$ can be determined.

Once the order parameters are known, it is possible to infer what is the most probable ODF consistent with the observed $\langle P_2 \rangle$ and $\langle P_4 \rangle$. Assuming that the anisotropy in the system is produced in a smooth way, the "smoothest" distribution is taken as the best approximation to the "most probable" distribution.[44]

It is possible to calculate $F(\theta)$ by using the information entropy of orientation S as:[43,44,50]

$$S(F(\theta)) = -\int_{-1}^{+1} F(\theta)\ln(F(\theta))\mathrm{d}(\cos\theta) \quad (4)$$

Maximization of the information entropy by use of the Lagrange multipliers method gives access to the distribution function:

$$F(\theta) = Z^{-1}\exp[\lambda_2 P_2(\cos\theta) + \lambda_4 P_4(\cos\theta)] \quad (5)$$

where λ_2 and λ_4 are the Lagrange multipliers and Z^{-1} is a normalization constant.

Simultaneous knowledge of the first two even Legendre parameters gives a qualitative insight into the mean orientation and the ODF shape. The order parameters are not completely independent and are restricted to values obeying the Schwartz inequalities:[43,46]

$$\langle \cos^2\theta \rangle^2 \leq \langle \cos^4\theta \rangle \leq \langle \cos^2\theta \rangle, \quad (6)$$

or equivalently for the associated Legendre polynomials (see eqn (2) and (3)).

$$\langle P_4 \rangle_{\min} \equiv \frac{1}{18}\left(35\langle P_2 \rangle^2 - 10\langle P_2 \rangle - 7\right) \leq \frac{1}{12}(5\langle P_2 \rangle + 7) \equiv \langle P_4 \rangle_{\max} \quad (7)$$

4 Results

4.1 Polarized Raman imaging of surface relief gratings (SRGs)

The Raman spectra acquired from the polymer films show essentially only vibrational bands which are assigned to the photo-sensitive azobenzene groups. Pre-resonance Raman effects play an important role in the enhancement of intensities of the chromophore vibrational bands.[51] In Fig. 6 a typical Raman spectrum as collected for the azobenzene containing polymer film grating is displayed. The inset shows the assignment for the most intense peaks of the azobenzene. The frequencies in wavenumbers and the intensities of the bands match very well with the spectra reported in the literature for the azobenzene molecule in *trans* configuration.[52] The *trans*-azobenzene has 66 fundamentals that span the representation $\Gamma = 33A_g + 33A_u$ vibrations and has an inversion centre, so $33A_g$ modes are Raman and $33A_u$ modes are IR active. In Table 1 (ref. 52) a summary of the bands along with the assignment is given. In the spectrum several vibrational modes are clearly identified (Fig. 6), *e.g.* ν(C–N) at 1148 cm^{-1}, ν(N=N) at 1440 cm^{-1}, and ν(C–C) at 1590 cm^{-1}.

From the optical microscopy image (Fig. 7(a)) the $\Lambda = 2$ μm periodic structure of the grating can be seen and it is possible to identify the top of each hill, slopes, and valleys of the SRG. Confocal polarized Raman microscopy has been applied to the grating sample inscribed with ±45° polarization combination.

Fig. 7(b) shows a section of the video image mapped with the Raman microscope. The Raman scattered intensity was obtained by integration of the chromophore band centered at 1148 cm^{-1}. The signal-to-noise ratio for these bands was high enough to use them as diagnostic signals for the detection of

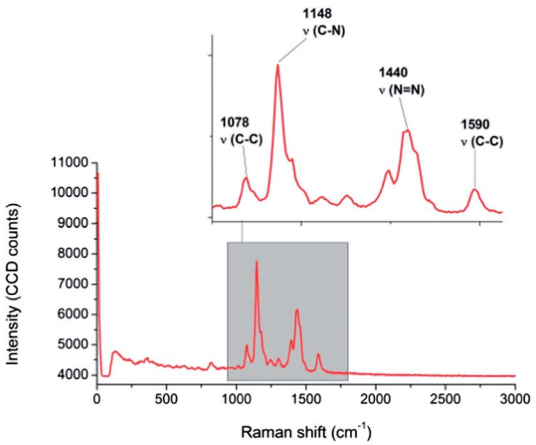

Fig. 6 Spectrum recorded on the polymer film surface. In the inset the most intense bands are shown with assignments (see Table 1).

Table 1 Peak[52] position and assignment of *trans*-azobenzene vibrations in the region from 1000 to 1600 cm^{-1}

Character	Frequency (cm^{-1})	PED[a] (%)
ν(C–C)	1071	63 ν(C–C), 16 δ(C–C), 10 δ(C–N), 10 δ(C–H)
ν(C–N)	1146	38 ν(C–N), 24 ν(C–C), 21 δ(C–C)
δ(C–H)	1158	53 δ(C–H), 45 ν(C–C)
ν(C–C)	1184	35 ν(C–C), 31 ν(C–N), 15 δ(C–C), 13 δ(C–H)
δ(C–H)	1315	39 δ(C–H), 24 δ(C–N), 17 ν(C–C)
ν(C–C)	1379	95 ν(C–C)
ν(N=N)	1443	54 ν(N=N), 25 ν(C–C)
ν(C–C)	1473	48 ν(C–C), 21 δ(C–N), 13 δ(C–H), 10 δ(C–C)
ν(C–C)	1493	38 ν(C–C), 27 ν (N=N), 17 δ(C–N), 11 δ(C–H)
ν(C–C)	1595	62 ν(C–C), 25 δ(C–C)

[a] PED: Potential Energy Distribution.

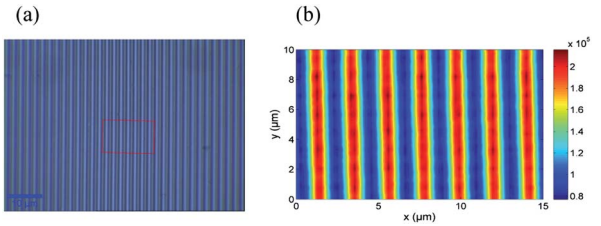

Fig. 7 (a) Optical microscopy image of the azo-polymer film, ±45° polarization grating, with a 100× magnification. (b) Unpolarized Raman image in the area indicated by the red rectangle in (a).

the chromophore in the polymer films. Analysis of different azobenzene group bands leads to similar results reproducing the SRG. The pattern reflects distinct scattering efficiencies of the sample along the grating periodicity.

In a different region of the sample a set of polarized images was measured. I_x and I_{yy} are shown in Fig. 8(a) and (c), respectively. Additional images for both experimental configurations (parallel and perpendicular to the SRG grooves) can be found in the ESI.† The images trace 12 μm along the X axis, corresponding to several grating periods, and 1 μm along the Y axis, and were recorded with longer integration time (1 s) to increase the signal-to-noise ratio. Four Raman images, two for each configuration, of the same sample were collected to obtain the depolarization ratios.

All images have been averaged along the Y axis (Fig. 8(b)). The resulting profiles of the Raman intensity have been fitted using a sinusoidal function. The fit reproduces the grating period of 2 μm for all Raman measurements.

The depolarization ratios have been evaluated in two different ways. First, we calculated the depolarization ratio $R_1 = I_{yx}/I_{yy}$ and $R_2 = I_{xy}/I_{xx}$ in the sampling area directly from the experimental data (Fig. 9(a) and (b)) followed by averaging along the Y axis. Secondly, the intensity ratios were evaluated from the ratio of the fitted profiles (Fig. 9(c)) as extracted from the intensity measurements shown in Fig. 8.

We recall that the intensity ratios R_1 and R_2 reflect combinations of the quantities ($\langle\cos^2\theta\rangle$ and $\langle\cos^4\theta\rangle$), which are

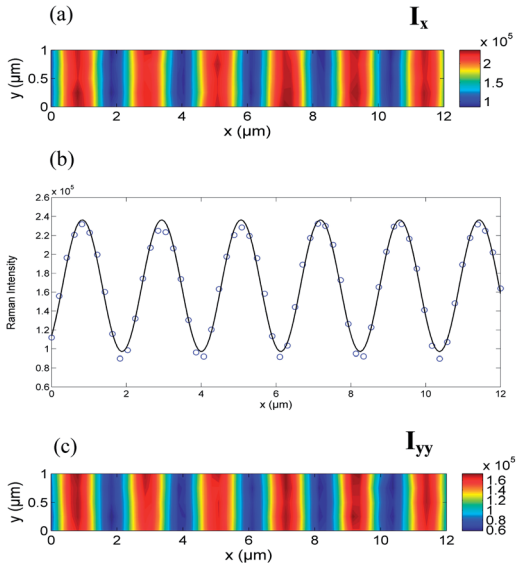

Fig. 8 ±45° polarization grating: (a) SRG Raman intensity of I_x imaged in the perpendicular configuration (without analyzer) and (b) experimental data along the X axis (circles) with a fitted optical profile (solid line). (c) Polarized Raman image (with analyzer) of the component I_{yy}.

averages of the distribution of orientations induced in the chromophores (see Section 3).

Whereas the experimental data points scatter, the overall trend is repeated over several grating periods and can be reproduced as seen in the fitted profiles. The range of variation is small, *i.e.* 0.31–0.36 for R_1 and 0.33–0.4 for R_2, but a clear trend is observed. A dephasing of nearly π exists between R_1 and R_2. The latter R_2 is found to be almost in phase with the SRG

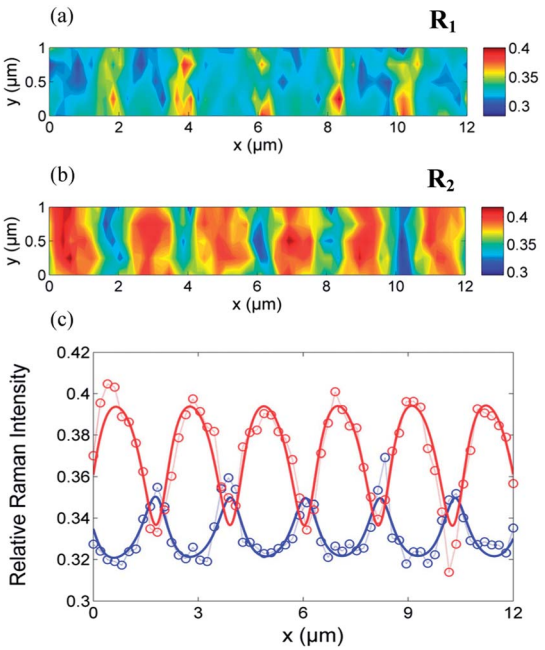

Fig. 9 Depolarization ratio (a) R_1 and (b) R_2 and (c) experimental data (open circles) and fitted profiles (solid line) along the X axis of R_1 (blue) and R_2 (red).

morphology. The oscillations of R_1 and R_2 with the phase of the grating indicate the existence of diverse orientation distributions at distinct positions of the photoinduced grating.

4.2 Polarization analysis of polymer films in the third dimension

The Raman images (Fig. 10(a)) show that the optical sectioning leads to a pattern composed of "egg"-shaped objects located underneath the surface. The calculation of the ratios R_1 and R_2 has been restricted to the region, where we can locate the polymer film and where the Raman signal is strong enough to give reliable values. The results shown in Fig. 10(b) and (c) indicate that the reorientation of the chromophores affects the entire film, even below the surface.

At each depth, the intensity follows a periodic change, which increases from the valley to the top of the grating, even inside the sample. The two ratios R_1 and R_2 are out of phase by π at the polymer–air surface and inside the sample. Both ratios increase with increasing distance from the grating surface being largest at the interface at z equal to zero (Fig. 10), which corresponds to the side of the inscription.

The most intense Raman signals for all the images (with parallel and perpendicular polarizations) are located at around $z = 0.8$ μm, in the center of the analyzed maps. $R_1(x,z)$ and $R_2(x,z)$ change with x and also with z, that is with the position along the grating and with the depth in the material.

4.3 Near-field microscopy with nanometre resolution

Grating fabricated with a SP interference pattern has been investigated by means of scanning near-field optical microscopy (SNOM).

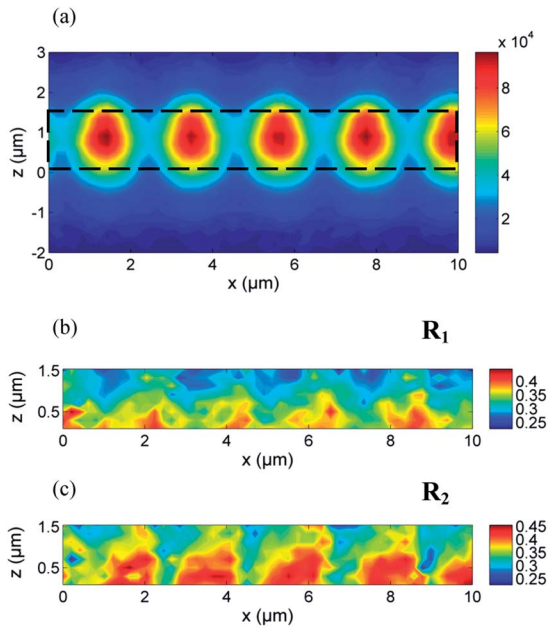

Fig. 10 Optical sectioning of the ±45° polarization grating. (a) Polarized Raman image of I_{yy}. (b and c) Derived images of R_1 and R_2 evaluated inside the marked region of (a) (black dashed rectangle).

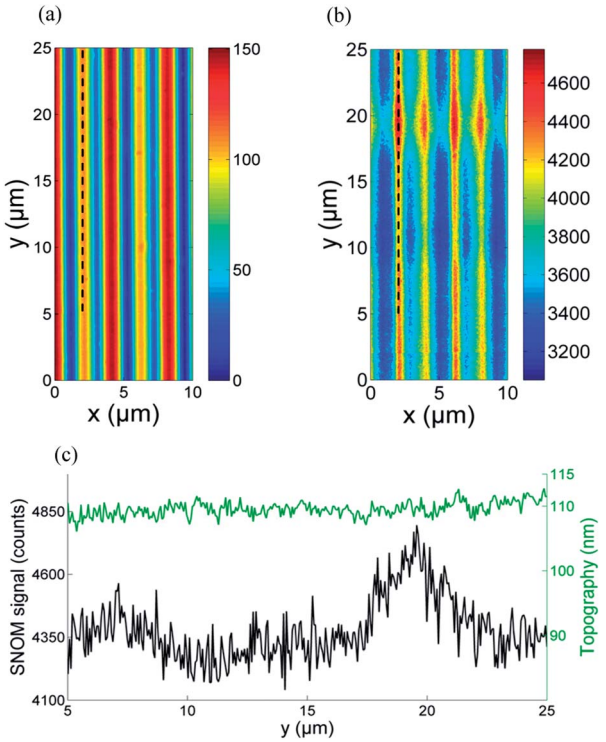

Fig. 11 SP polarization grating: (a) topography (in nm) showing two alternating gratings of different heights. (b) APD counts of the SNOM signal showing a two-dimensional optical contrast: regular along the X and irregular along the Y axis. (c) Topography (green) and SNOM signal (black) profile corresponding to the lines in (a) and (b).

Fig. 11(a) shows the topography of the grating in the scanned area in which two adjacent top hills differ by about 40 nm. Along the x direction the grating in the topographic image can be reproduced with two alternating gratings and with a spacing of 2 μm and 4 μm. In the direction parallel to the stripes of the grating the image is largely uniform. The SRG modulation is unidimensional and almost perfectly replicated along the X direction.

In contrast, the SNOM image (Fig. 11(b)) reveals a two-dimensional optical near-field contrast in the Y direction for which the topography is flat (Fig. 11(c)). The stripes in the near-field image are narrower, if compared to the topography, and localized at the centre of the hills. The width of these features changes: in the upper part of Fig. 11 the width is about 1 μm and 0.7 μm for the two distinct gratings. In the centre of the image a width of 0.4 and 0.3 μm is found, respectively.

Near-field microscopy reveals, in addition to the one-dimensional grating structure, a structure perpendicular to the grating, and thus a two-dimensional optical contrast of the material while AFM and Raman microscopy only reveal one-dimensional contrast along the grating.

4.4 Evaluation of the order parameters and relative orientation distribution functions from the surface into the bulk polymer

Based upon the measured depolarization ratios we have been able to calculate the averaged quantities $\langle\cos^2\theta\rangle$ and $\langle\cos^4\theta\rangle$

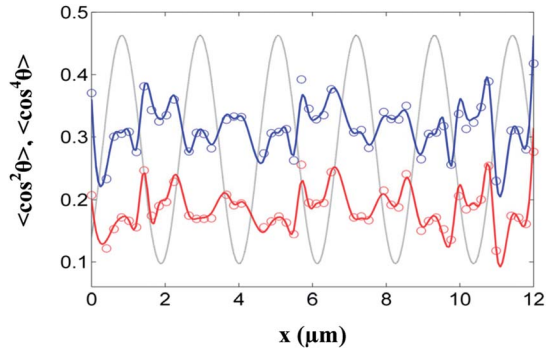

Fig. 12 $\langle \cos^2 \theta \rangle$ (blue line) and $\langle \cos^4 \theta \rangle$ (red line) as a function of x, experimental data (open circles), fitted lines (solid), and grating topography within the scanned area (solid gray line).

and derive the order parameters $\langle P_2 \rangle$ and $\langle P_4 \rangle$ (see eqn (3) and Section 3 for details). In Fig. 12 the average cosines derived from the data shown in Fig. 9(c) are displayed.

The top-hills, slopes, and bottoms of the SRG are characterized by distinct orientational coefficients, due to the chromophore reorientation during the grating formation. Eqn (6) and (7) (see Section 3) set limits to the available range of order parameters.

The domain of acceptance of $\langle P_2 \rangle$ and $\langle P_4 \rangle$ can be divided into sectors describing, *e.g.*, different ODFs such as cone, Gaussian, or isotropic distributions. Here, the polymer films have order parameters with small values. Their correlation is shown in a $\langle P_4 \rangle$ *versus* $\langle P_2 \rangle$ correlation diagram[43–45] (Fig. 13) derived from the cosines (Fig. 12).

Four characteristic groups are identified, each located in a specific region of the $\langle P_2 \rangle - \langle P_4 \rangle$ plane, each corresponding to specific SRG regions. Using continuous lines derived from fitting the depolarization ratios from the data (Fig. 9), we can virtually increase the sampling and highlight the data density of the order parameters (Fig. 14).

The cluster at the center of the correlation scatter plot and histogram (Fig. 13 and 14) corresponds to the SRG bottom and

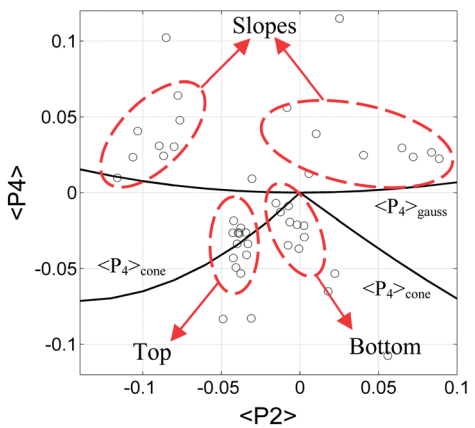

Fig. 13 $\langle P_2 \rangle - \langle P_4 \rangle$ correlation diagram of the measured data forming clusters, each corresponding to a distinct SRG regions and sectors defining specific ODFs such as cone, Gaussian and isotropic distributions.

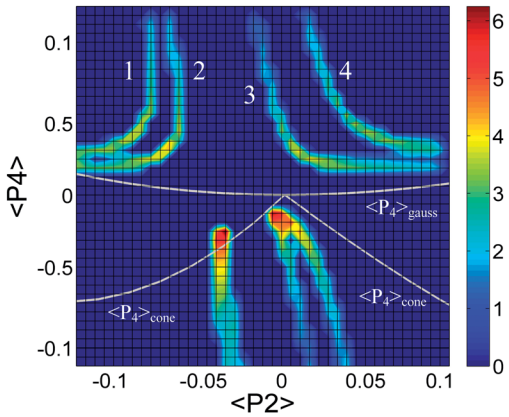

Fig. 14 $\langle P_2 \rangle - \langle P_4 \rangle$ correlation histogram of the occurrence frequency derived from sampling the fitted curves (Fig. 9) using 10 000 points displayed in the interpolated logarithmic scale.

is characterized by $\langle P_2 \rangle$ values close to zero and small negative $\langle P_4 \rangle$ indicating a nearly isotropic ODF – the origin of $\langle P_2 \rangle - \langle P_4 \rangle$ plane stands for isotropy. The cluster corresponding to the SRG top hills has larger negative $\langle P_2 \rangle$ and $\langle P_4 \rangle$ values. This cluster is best described by a cone distribution (Fig. 14). The cone distribution is depicted in the correlation diagram as two lines crossing in the origin. The cone distribution corresponds to molecules oriented within a cone centered at a specific angle. The SRG slopes form four branches 1–4 (Fig. 14) in the $\langle P_2 \rangle - \langle P_4 \rangle$ plane, branches 3 and 4 with mostly positive $\langle P_2 \rangle$ and branches 1 and 2 with negative $\langle P_2 \rangle$, but $\langle P_4 \rangle$ values are always positive. The points are located in the section of the $\langle P_2 \rangle - \langle P_4 \rangle$ plane above the Gaussian distribution line. Here the diagram displays a bimodal distribution with two maxima at 0° and 90°. The relative intensity depends on the precise values of $\langle P_2 \rangle$ and $\langle P_4 \rangle$. All branches 1–4 approach in part the line characterizing an ideal Gaussian ODF. The correlation diagram of the order parameters shows that the photoinduced reorientation mechanism and the interplay of mass transport in the polymer film create periodic domains with different reorientation extent and order.

In order to analyze the various molecular domains arranged in the system we evaluate the most probable ODFs by means of maximization of the information entropy.[34,37,43,44]

In Table 2 we report the values of the calculated Lagrange multipliers in distinct regions of the grating along with the corresponding order parameters and the averaged cosines

Table 2 Average cosines, order parameters, and Lagrange multipliers at distinct SRG positions[a]

δ	$\langle \cos^2 \theta \rangle$	$\langle \cos^4 \theta \rangle$	$\langle P_2 \rangle$	$\langle P_4 \rangle$	λ_2	λ_4
0	0.31	0.17	−0.04	−0.02	−0.22	−0.24
$\pi/5$	0.31	0.16	−0.04	−0.07	−0.29	−0.70
$2\pi/5$	0.26	0.15	−0.10	0.03	−0.55	0.18
$3\pi/5$	0.37	0.24	0.06	0.02	0.26	0.17
$4\pi/5$	0.34	0.20	0.01	−0.04	0.05	−0.38
π	0.33	0.19	0.00	−0.01	−0.02	−0.12

[a] Values are averages of points located at the same phase of the grating.

values at the same position. The corresponding normalized distributions in polar coordinates are shown in Fig. 15.

λ_2 and λ_4 have been derived for the entire dataset and were grouped in dependence of the relative phase along the grating. Similar to $\langle P_2 \rangle$ and $\langle P_4 \rangle$, the estimated Lagrange multipliers indicate that the molecular organization is highly affected by photoinduced reorientation. λ_2 shows a significant phase dependency changing sign from negative at the SRG top hills ($\delta = 0$, $\pi/5$ and $2\pi/5$) to positive ($\delta = 3\pi/5$) and almost 0 at the bottom. Here the ODF is essentially determined by the value of λ_4, which is negative at the top and bottom, and positive at the slope. Thus we conclude that on the SRG top the molecules are arranged in an asymmetric unimodal distribution with a preferential molecular alignment at 90°, albeit the maximum is centered around 55°. The overall orientation is more pronounced at $\delta = \pi/5$ (and $\delta = 2\pi - \pi/5 = 9\pi/5$) than at the top ($\delta = 0$) where the distribution appears more uniform. Surprisingly, on the slopes we find the most effective orientation, in fact, the distribution shows two maxima located at 0° and 90°. At $\delta = 2\pi/5$ (and $8\pi/5$) we find a preferred 90° orientation while at $\delta = 3\pi/5$ (and $7\pi/5$) the 0° orientation is most pronounced.

The polarization interference pattern of the pump beam (Fig. 5) is linearly polarized at $\delta = 0$ and $\delta = \pi$, circularly polarized at $\delta = \pi/2$ and $\delta = 3\pi/2$ and elliptically polarized otherwise. Here we find that the ODFs resemble the polarization state of the actinic light in the chromophore reorientation. For the SRG slopes the molecular orientation appears to be remarkably affected by the photoisomerization process. In the region at the SRG bottom the polar plots show very little orientational effect (Fig. 15). The ODF is nearly isotropic at $\delta = \pi$ exhibiting a slightly asymmetric unimodal distribution at $\delta = 4\pi/5(6\pi/5)$ with a maximum angle located at around 47°.

In contrast to previous reports,[36,37] we find orientational effects at all positions on the surface of the film, although the resulting chromophore redistribution is quite smooth for all grating positions. However in the back illumination scheme implemented for the grating inscription, the light intensity is rather low on the free surface and a high degree of topography change is probably caused mainly by chain migration from the inner part of the film. We can expect that the photoswitching processes are much less effective on the surface where the grating relief is developed, and in this case, mass transport considerably influences the molecular domain organization.

To further corroborate these conclusions we have calculated the most probable ODF at diverse depths inside the sample. Starting from the depolarization ratios found in the optical sectioning of the azo-film (Fig. 10(b) and (c)), we have analyzed the order parameters and the subsequent ODF along the film thickness (Table 3). Fig. 16 shows the evolution of the molecular orientation with depth at specific SRG positions: on top ($\delta = 0$) and at the bottom ($\delta = \pi$).

The results presented in Table 3 and the ODFs of Fig. 16 are averaged values of equivalent points in the Raman maps (*i.e.* $\delta = 2\pi n$ for top and $\delta = 2\pi n + \pi$ for bottom).

We find that the anisotropy is not restricted to the upper surface of the sample, indeed an anisotropic distribution is

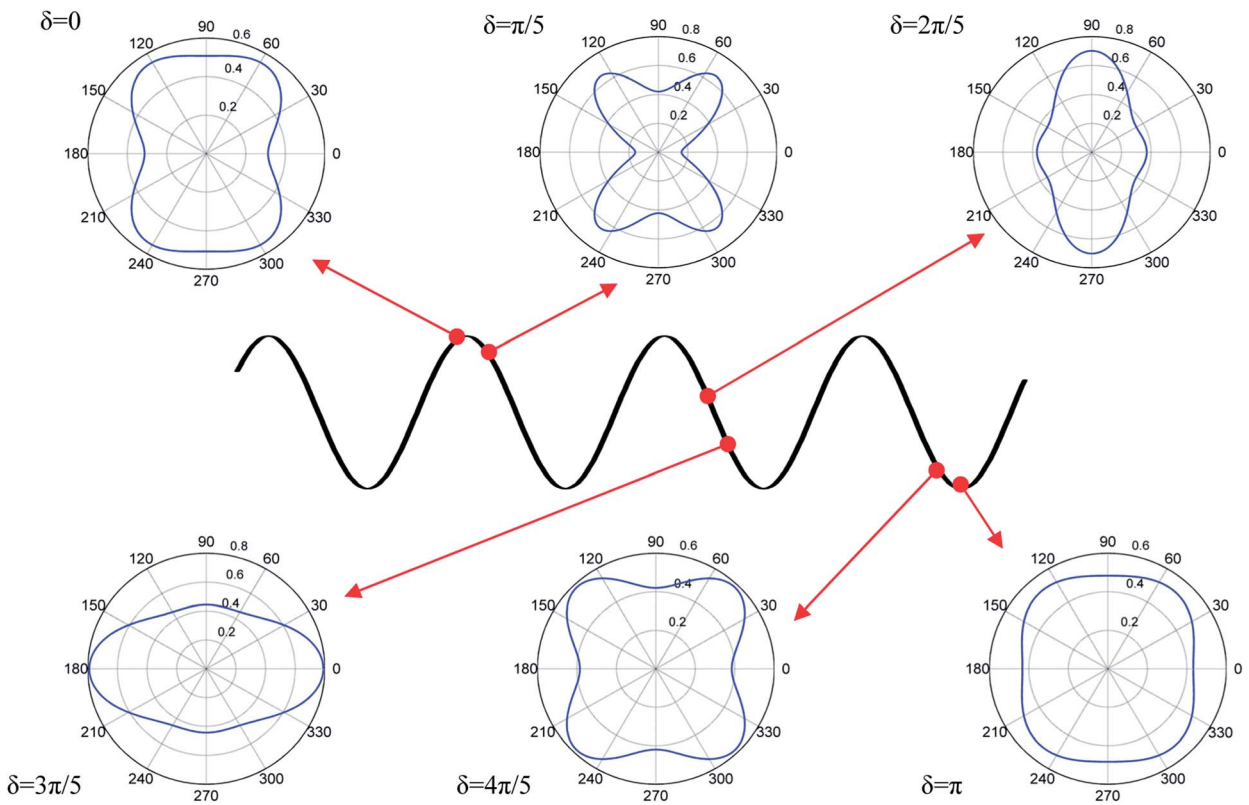

Fig. 15 Polar plot of $F(\theta)$, the calculated ODF corresponding to several SRG regions at the phase $\delta = 0$, $\pi/5$, $2\pi/5$, $3\pi/5$, $4\pi/5$, and π.

Table 3 Average cosines, order parameters, and Lagrange multipliers at distinct depths[a]

		$\langle\cos^2\theta\rangle$	$\langle\cos^4\theta\rangle$	$\langle P_2\rangle$	$\langle P_4\rangle$	λ_2	λ_4
	z^b/μm						
$\delta = 0$	1.2	0.31	0.18	−0.04	−0.01	−0.19	−0.12
	0.6	0.31	0.17	−0.03	−0.04	−0.16	−0.38
	0	0.31	0.16	−0.03	−0.07	−0.22	−0.69
$\delta = \pi$	1.2	0.33	0.19	−0.01	0.00	−0.04	−0.02
	0.6	0.31	0.18	−0.03	−0.01	−0.17	−0.15
	0	0.32	0.18	−0.01	−0.03	−0.09	−0.32

[a] Values are averages of points located at the same phase of the grating. [b] $z = 1.2$ μm, 0.6 μm and 0 μm correspond to the top air–polymer interface, the middle and the bottom polymer–glass interface of the SRG film.

found for all investigated z-values, and involves the complete thickness of the film (Fig. 16). The reorientation of chromophores is even more pronounced inside the sample than on the surface and shows the strongest effect at the lower polymer–glass interface. In both analyzed regions of the grating, $\delta = 0$ and $\delta = \pi$, the ODF anisotropy is increased while moving further inside the sample: nearly isotropic distribution at the upper surface, and more peaked distribution on the opposite surface, thus indicating an increased ordering of the molecular domains with depth.

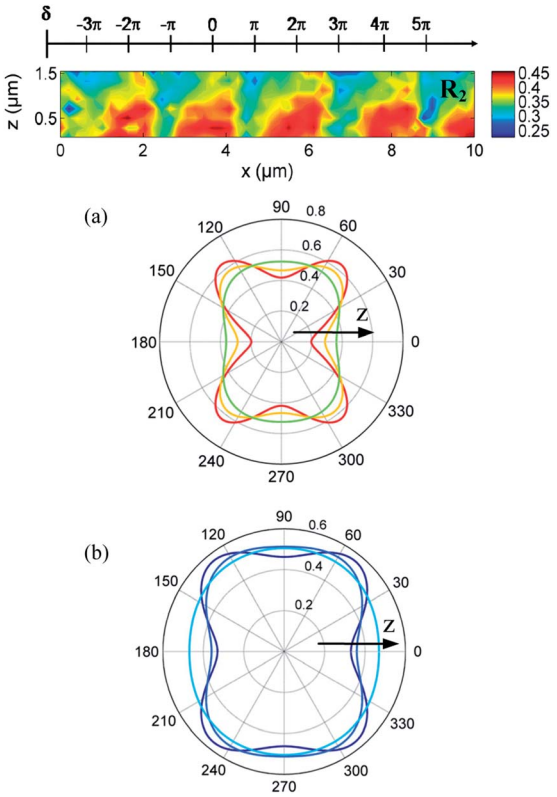

Fig. 16 Polar plots of $F(\theta)$ calculated at the upper surface ($z = 1.2$ μm), film center ($z = 0.6$ μm), and lower surface ($z = 0$ μm) at SRG positions (a) $\delta = 0$ and (b) $\delta = \pi$. The arrows indicate increasing z values for the ODFs. The colors in both polar plots roughly correspond to the same colors in R_2.

A closer look at the coefficients in Table 3 reveals which factors influence the change in $F(\theta)$. At phase $\delta = 0$, the $\langle\cos^2\theta\rangle$, $\langle P_2\rangle$, and λ_2 values remain constant. In contrast $\langle P_4\rangle$ and λ_4, although remaining small, decrease with depth and mainly determine the change of the ODF. At phase $\delta = \pi$, the situation is different, because both the order parameters and the λ multipliers are smaller inside the material than at the interfaces, although only $\langle P_4\rangle$ and λ_4 monotonically decrease.

Our results can be explained, if we consider that the laser radiation used to inscribe the grating in the photosensitive material has to penetrate the film. Photon absorption and hence photoinduced reorientation of the chromophores take place at the surface and inside the sample, and we expect the highest photoreaction rate at the glass–polymer interface.

In a three-dimensional approach, the orientation function of the photo-sensitive molecules varies in the plane of the film with the period of the inscribed grating and with the distance from the surface. The reorientation phenomena indicate not only molecular reorganization, but also a strong uniaxial stress inside the sample, which is responsible for mass transport of the macromolecules. Here we want to mention the models developed by Saphiannikova and Toshchevikov[53,54] in which the authors describe how the actinic light produces stress in the material that acts like a driving force for mass transport and reorientation of the molecular axis of chromophores. We believe that our results prove that in the bulk of the film, where the light intensity is high, a large molecular reorientation is achieved and a strong uniaxial stress is produced. At the free surface of the sample, where the light intensity is small, the molecular reorientation is mainly due to the uniaxial stress related to grating formation.

5 Conclusions

Using polarized confocal Raman microscopy we were able to measure the reorientational phenomena inscribed in the sample by the chromophore response to the actinic light. We have successfully determined the orientational distribution functions (ODFs) in several regions of the surface relief grating (SRG) illustrating different reorientation processes at the top, slopes and bottom of the grating during the photoinduced mass transport. These changes are found to be correlated with topographical changes. We conclude that the anisotropy induced in the sample is the result of distinct orientation distributions in different grating regions. Although the overall alignment of chromophores is barely pronounced, the redistribution of the azo-dyes shows clear features: the orientation distribution of chromophores remains almost isotropic at the bottom of the grating, on the top region the ODF shows an asymmetric maximum at 55° relative to the actinic light and on the slopes we find a more marked redistribution.

Optical sectioning of the samples has been performed to elucidate the role of the bulk material in mass migration. Polarized Raman measurements allowed us to extract the molecular orientation functions revealing a larger degree of anisotropy inside the material than on the air–polymer surface. Confocal polarized Raman imaging has been used to

characterize the reorientation of molecules and the structure of photoinduced molecular domains in 3D.

We could quantify the three-dimensional molecular anisotropy of these materials from the surface into the bulk thin film and at the two interfaces. We conclude that the SRG inscription involves photo-sensitive molecules at the free surface as well as in the bulk material and at the polymer–substrate interface. This reorientation causes stress, mass migration and grating formation.

Near-field optical measurements with high spatial resolution of 60 nm using SNOM showed that the optical inscription of surface gratings also creates lateral two-dimensional optical contrast, which may be due to fine intensity modulations of the interfering beams, in contrast to well-defined periodic structures in one, the grating direction. These fine details have not been observed before when using surface AFM or confocal Raman microspectroscopy.

Acknowledgements

We like to acknowledge the DFG for financial support in the framework of the Priority Program 1369 "Polymer-Solid Contacts: Interfaces and Interphases" under HA 2394/23-1. The confocal Raman and near-field optical microscope was supported by Deutsche Forschungsgemeinschaft (DFG) by the programme "Großgeräte der Länder".

References

1 J. L. Keddie, R. A. L. Jones and R. A. Cory, *Europhys. Lett.*, 1994, **27**, 59.
2 C. B. Roth, K. L. McNerny, W. F. Jager and J. M. Torkelson, *Macromolecules*, 2007, **40**, 2568.
3 J. A. Forrest, K. Dalnoki-Veress and J. R. Dutcher, *Phys. Rev. E: Stat., Nonlinear, Soft Matter Phys.*, 1997, **56**, 5705.
4 R. H. Berg, S. Hvilsted and P. S. Ramanujam, *Nature*, 1996, **383**, 505.
5 S. J. Zilker, T. Bieringer, D. Haarer, R. S. Stein, J. W. van Egmond and S. G. Kostromine, *Adv. Mater.*, 1998, **10**, 855.
6 A. Stracke, J. H. Wendorff, D. Goldmann, D. Janietz and B. Stiller, *Adv. Mater.*, 2000, 282.
7 D. Sainova, A. Zen, H.-G. Nothofer, U. Asawapirom, U. Scherf, R. Hagen, T. Bieringer, S. Kostromine and D. Neher, *Adv. Funct. Mater.*, 2002, **12**, 49.
8 A. Zen, D. Neher, C. Bauer, U. Asawapirom, U. Scherf, R. Hagen, S. Kostromine and R. F. Mahrt, *Appl. Phys. Lett.*, 2002, **80**, 4699.
9 A. Natansohn and P. Rochon, *Adv. Mater.*, 1999, **11**, 1387.
10 H. Tachibana, T. Nakaura, M. Matsumoto, H. Komizu, E. Manda, H. Niino and A. Yabe, *J. Am. Chem. Soc.*, 1989, **11**, 3080.
11 M. Dumont, G. Froc and S. Hosotte, *MCLC S&T, Sect. B: Nonlinear Opt.*, 1995, **9**, 327.
12 T. Todorov, L. Nikolova and T. Tomova, *Appl. Opt.*, 1984, **23**, 4309.
13 C. Jones and S. Day, *Nature*, 1991, **15**, 351.
14 F. Lagugné Labarthet, T. Buffeteau and C. Sourrisseau, *J. Phys. Chem. B*, 1998, **102**, 2654.
15 C. J. Barrett, J. Mamiya, K. G. Yager and T. Ikeda, *Soft Matter*, 2007, **3**, 1249.
16 X. L. Jang, L. Li, J. Kumar, D. Y. Kim, V. Shivshankar and S. K. Tripathy, *Appl. Phys. Lett.*, 1996, **68**(19), 2618.
17 N. K. Viswanathan, D. Y. Kim, S. Bian, J. Williams, W. Liu, L. Li, L. Samuelson, J. Kumar and S. K. Tripathy, *J. Mater. Chem.*, 1999, **9**, 1941.
18 R. Loucif-Saibi, K. Nakatani, J. A. Delaire, M. Dumont and Z. Sekkat, *Chem. Mater.*, 1993, **5**, 229–236.
19 H. Rau and E. Lüddecke, *J. Am. Chem. Soc.*, 1982, **104**, 1616.
20 Y. Morikawa, S. Nagano, K. Watanabe, K. Kamata, T. Iyoda and T. Seki, *Adv. Mater.*, 2006, **18**, 883.
21 T. Uekusa, S. Nagano and T. Seki, *Langmuir*, 2007, **23**, 4642.
22 J. Stumpe, Th. Geue, Th. Fischer and H. Menzel, *Thin Solid Films*, 1996, **284–285**, 606.
23 Th. Geue, U. Pietsch and J. Stumpe, *Thin Solid Films*, 1996, **284–285**, 228.
24 Z. Sekkat and M. Dumont, *Appl. Phys. B*, 1991, **53**, 121.
25 C. Fiorini, N. Prudhomme, A. C. Etilé, P. Lefin, P. Raimond and J. M. Nunzi, *Macromol. Symp.*, 1999, **137**, 105.
26 P. Lefin, C. Fiorini and J. M. Nunzi, *Pure Appl. Opt.*, 1998, **7**, 71.
27 T. G. Pedersen, P. M. Johansen, N. C. R. Holme, P. S. Ramanujam and S. Hvilsted, *Phys. Rev. Let.*, 1998, **80**(1), 89.
28 T. G. Pedersen and P. M. Johansen, *Phys. Rev. Lett.*, 1997, **79**(13), 2470.
29 C. J. Barrett, A. L. Natansohn and P. L. Rochon, *J. Phys. Chem.*, 1996, **100**, 8836.
30 C. J. Barrett, P. L. Rochon and A. L. Natansohn, *J. Chem. Phys.*, 1998, **109**, 1505.
31 T. Fukuda, K. Sumaru, T. Yamanaka and H. Matsuda, *Mol. Cryst. Liq. Cryst. Sci. Technol., Sect. A*, 2000, **345**, 263.
32 B. Bellini, J. Ackermann, H. Klein, Ch. Grave, Ph. Dumas and V. Safarov, *J. Phys.: Condens. Matter*, 2006, **18**, 1817.
33 F. Lagugné Labarthet and C. Sourrisseau, *J. Raman Spectrosc.*, 1996, **27**, 491.
34 F. Lagugné Labarthet, T. Buffeteau and C. Sourrisseau, *J. Phys. Chem. B*, 1998, **102**, 5754.
35 F. Lagugné Labarthet, C. Sourrisseau, R. D. Schaller, R. J. Saykally and P. Rochon, *J. Phys. Chem. B*, 2004, **108**, 17059.
36 F. Lagugné Labarthet, J. L. Bruneel, T. Buffeteau, C. Sourrisseau, M. R. Huber, S. J. Zilker and T. Bieringer, *Phys. Chem. Chem. Phys.*, 2000, **2**, 5154.
37 F. Lagugné Labarthet, J. L. Bruneel, T. Buffeteau and C. Sourrisseau, *J. Phys. Chem. B*, 2004, **108**, 6949.
38 N. S. Yadavalli and S. Santer, *J. Appl. Phys.*, 2013, **113**, 224304.
39 N. S. Yadavalli, M. Saphiannikova, N. Lomadze, L. M. Goldenberg and S. Santer, *Appl. Phys. A*, 2013, **113**, 263.
40 S. Lee, Y. C. Jeong and J. K. Park, *Appl. Phys. Lett.*, 2008, **93**, 031912.
41 J. H. Nobbs, D. I. Bower and I. M. Ward, *J. Polym. Sci., Polym. Phys. Ed.*, 1979, **17**, 259.

42 J. Purvis and D. I. Bower, *J. Polym. Sci., Polym. Phys. Ed.*, 1976, **14**, 1461.
43 H. Pottel, W. Herreman, B. W. van der Meer and M. Ameloot, *Chem. Phys.*, 1986, **102**, 37.
44 D. I. Bower, *J. Polym. Sci., Polym. Phys. Ed.*, 1981, **19**, 93.
45 S. Nomura, N. Nakamura and H. Kawai, *J. Polym. Sci., Part A: Polym. Chem.*, 1971, **9**, 407.
46 C. Sourrisseau, *Chem. Rev.*, 2004, **104**, 3851.
47 G. Placzek, *Handbuch der Radiologie*, ed. E. Marx, Akad. Verlag, Leipzig, 1934, vol. VI-2.
48 D. A. Long, *Raman Spectroscopy*, McGraw-Hill, New York, 1977; D. A. Long, *The Raman Effect: a unified treatment of the theory of Raman scattering by molecules*, John Wiley, Chichester, U.K, 2002.
49 S. Nomura, H. Kawai, I. Kimura and M. Kagiyama, *J. Polym. Sci., Part A: Polym. Chem.*, 1970, **8**, 383.
50 B. J. Berne, P. Pechukas and G. D. Harp, *J. Chem. Phys.*, 1968, **49**, 3125.
51 N. Biswas and S. Umapathy, *J. Chem. Phys.*, 1997, **107**, 7849.
52 N. Biswas and S. Umapathy, *J. Phys. Chem. A*, 1997, **101**, 5555.
53 M. Saphiannikova and D. Neher, *J. Phys. Chem. B*, 2005, **109**, 19428.
54 V. Toshchevikov, M. Saphiannikova and G. Heinrich, *J. Phys. Chem. B*, 2009, **113**, 5032.